

Realization of acoustic tunable logic gate composed of soft materials

Yuanyuan Li ^a, Kunqi Huang ^a, Menyang Gong ^a, Chenghao Sun ^a, Shenlian Gao ^a, Yun Lai ^a, Xiaozhou Liu ^{a,b,*}

^a Key Laboratory of Modern Acoustics, Institute of Acoustics and School of Physics, Collaborative Innovation Center of Advanced Microstructures, Nanjing University, Nanjing 210093, China

^b State Key Laboratory of Acoustics, Institute of Acoustics, Chinese Academy of Sciences, Beijing 100190, China

ARTICLE INFO

Keywords:
Acoustic
Logic gate
Metamaterial
Tunable

ABSTRACT

Acoustic logic gates have emerged as a prominent research focus, but once their structures are designed, the properties of these logic gates become challenging to alter, exhibiting a fixed nature. In response to the aforementioned issue, here we propose acoustic logic gates composed of soft materials that are tunable via external mechanical control. The external tunability of bandgaps in chiral-ligament phononic crystals (PnCs) with both C-tentaclelike (C-T) and S-tentaclelike (S-T) structures is explored. The results reveal that under the same mechanical strain, both structures exhibit an on/off transition effect in their bandgaps, but with distinct characteristics. As an extension, a reconfigurable bidirectional acoustic switching device and an acoustic channel are constructed, enabling tunable applications. Especially, a tunable acoustic logic gate is proposed and experimentally demonstrated, which allows for dynamic alterations of its logical attributes through external stretching. Our findings not only hold applicability in acoustic wave manipulation and noise reduction, but also demonstrate great potential in acoustic designs based on soft and flexible materials.

Introduction

Attributing to the extensive research on acoustic metamaterials and the development of acoustic wave manipulation, various acoustic functional devices have been proposed and become research hotspots, such as acoustic switches [1,2], filters [3–5], waveguides [6] and logic gates [7–12]. Among these, acoustic logic gates refer to structures or devices that perform Boolean logic operations on two or more acoustic signals. Building upon previous studies on optical logic gates [13–16], Bringuiel et al. [7] first introduced the concept of acoustic Boolean operation logic. They designed a system where two counter-propagating control waves with opposite phases in a phononic crystal (PnC) caused a reduction in the overall acoustic field through linear interference between the input and control signals in the PnC. Apart from logic gates based on linear interference [8], there have also been studies on logic gates based on nonlinear interference [1]. Subsequently, some researchers proposed the realization of acoustic logic gates based on the self-collimation effect [9–11], overcoming certain drawbacks of interference-based acoustic logic gates, such as the inability to compute complex logic gates and the complexity of signal frequencies in emission and reception. Nevertheless, the problem of fixed logic gate mode under a designed single structure still persists, which is one of the main issues addressed in this paper.

PnCs, for the most part, exhibit fixed band gaps after structural design, which has led to considerable interest in the study of PnC band gap tuning across various application domains [17–25]. Goffaux et al. [17] pioneered the concept of a tunable PnC achieved through the rotation of solid scatterers. Jin et al. [24,25] tuned the acoustic wave transmission and Bragg band gap by filling the hollow pillars with a liquid. Some methods involved indirectly altering the material properties or geometric structure through the stimulation of environmental variables like applying a static magnetic field [18], using infrared electromagnetic radiation [19], using temperature-sensitive materials [20], and connecting PnC to a resonant circuit with piezoelectric transducers [21]. These approaches came with high environmental requirements, limiting their practical applicability. Consequently, mechanical loading is the most common and easily controllable means of band gap tuning. Pre-stress and the large deformability of soft materials have garnered significant attention because such materials possess the ability to simultaneously modify their geometric shapes and material stiffness, offering reversible large deformations and diverse mechanical properties [22]. Beroldi et al. [26–29] investigated a range of periodic porous elastic structures, harnessing the instability and post-buckling deformation characteristics of soft materials to adjust band gap properties and

* Corresponding author at: Key Laboratory of Modern Acoustics, Institute of Acoustics and School of Physics, Collaborative Innovation Center of Advanced Microstructures, Nanjing University, Nanjing 210093, China.

E-mail addresses: laiyun@nju.edu.cn (Y. Lai), xzliu@nju.edu.cn (X. Liu).

wave propagation in elastic bodies through mechanical loading. Wang et al. [30] designed PnCs based on the principle of localized resonance, considering the effects of nonlinear pre-deformation on the propagation of elastic waves within structures utilizing the post-buckling effect. Ning et al. [31] embedded various resonant units, including soft elastic coating and a rigid core, into an elastic matrix, studying the influence of mechanical tuning on local resonance and Bragg scattering band gaps. The above-mentioned studies predominantly center on the buckling effects occurring when objects undergo elastic or plastic deformation due to external pressures or bending moments exceeding their load-bearing capacity. Buckling behavior is contingent upon material properties, geometric shapes, and applied forces. However, buckling effects exhibit multiple orders, and inducing corresponding orders of buckling behavior places stringent demands on applied forces. Consequently, chiral structures exhibiting typical negative Poisson's ratio characteristics have gradually become the focus of researches [32–37]. A typical chiral structure comprises two components: a central structure and link rod structures connected to the central. These structural units exhibit broken mirror symmetry and rotational symmetry, enabling chiral PnCs to alter phononic properties with minor deformations, leading to rich phononic bandgap characteristics and outstanding acoustic transmission and filtering capabilities [38,39].

In this paper, based on the external tunability of PnC bandgaps, a novel tunable acoustic logic gate structure is introduced. The fundamental unit of this structure is chiral ligamentous configurations composed of soft materials capable of withstanding significant deformations without damage. External control is achieved through stable mechanical stretching without buckling effects. The organization of this article is as follows: Section “Model and energy band response computation” proposes the model and elaborates on the wave characteristics of PnCs. Section “Effect of tensile stress on band gap” investigates the influence of mechanical stress on the bandgap properties of C-tentaclelike (C-T) and S-tentaclelike (S-T) structures, as well as simulation validation of the feasibility of reconfigurable acoustic switches and combinatory acoustic channels. Section “Logic gate conversion” leverages the two aforementioned structures to design and construct a tunable logic gate. In Section “Experiment”, an experimental system to validate the deformation patterns and control bandgap characteristics outlined in the preceding chapters is established. Furthermore, this pivotal chapter aims to demonstrate the rapid switching of acoustic logic gate functionalities experimentally.

Model and energy band response computation

The acoustic devices designed in this study are based on two chiral structures, each composed of four ligaments and a circular ring, as depicted in Figs. 1(a) and (b). These structures are referred to as the C-T structure and the S-T structure, with their distinction lying in the number of curvature segments in the ligaments. Consequently, the C-T structure and the S-T structure should exhibit different levels of bandgap richness and show varying bandgap closures and openings under applied stress, as will be demonstrated in subsequent research. The dimensions are as shown in the figures: w represents the ligament width, a is the distance between units, $L = 2a$, R is the radius of the central circular ring, and α and θ denote the angular degrees of curvature for the C-T structure and S-T structure, respectively.

The material in simulations is silicon rubber, a high-polymer nonlinear substance renowned for its softness and remarkable deformability. It falls under the category of hyperelastic materials. Among the various models for hyperelastic strain energy [40–43], the Neo-Hookean model [44] is frequently employed to describe materials exhibiting ligamentous behavior. Its constitutive equation is defined as follows:

$$W = C_{10}(\bar{I}_1 - 3) + \frac{1}{D_1}(J - 1)^2. \quad (1)$$

Here, W represents the strain energy density function, is the invariant of strain tensor, J is the volume ratio after and before deformation,

$C_{10} = G_0 / 2$, $D_1 = 2 / K_0$, while G_0 and K_0 stand for the initial shear modulus and initial bulk modulus, respectively. Employing this constitutive modeling approach effectively characterizes the material's deformation behavior, with the parameters C_{10} and D_1 assuming particular significance in subsequent finite element simulations and experimental assessments.

In the context of the finite element simulation employed, the research commences by dissecting the displacement increment into its real and imaginary components. This procedure involves the formulation of a series of instance models, each representing the real and imaginary aspects of the complex variable, culminating in a pair of elements. According to phonon crystal theory, large deformation structure governing equation based on macroscopic deformation and microscopic deformation, combined with the Bloch principle in Appendix A. The real and imaginary components of the displacement increment's Bloch conditions are articulated.

$$\dot{\mathbf{u}}^{re}(\mathbf{X} + \mathcal{A}) = \dot{\mathbf{u}}^{re}(\mathbf{x}_0) \cos(\mathbf{k}_k \cdot \mathcal{A}) - \dot{\mathbf{u}}^{im}(\mathbf{x}_0) \sin(\mathbf{k}_k \cdot \mathcal{A}), \quad (2)$$

$$\dot{\mathbf{u}}^{im}(\mathbf{X} + \mathcal{A}) = \dot{\mathbf{u}}^{re}(\mathbf{x}_0) \sin(\mathbf{k}_k \cdot \mathcal{A}) + \dot{\mathbf{u}}^{im}(\mathbf{x}_0) \cos(\mathbf{k}_k \cdot \mathcal{A}). \quad (3)$$

In the constructed model consisting of two unit cells, Bloch conditions, as illustrated in Eqs. (2) and (3), are imposed on the model boundaries. The soft material parameters are as follows: density $\rho = 1050 \text{ kg/m}^3$, $G_0 = 1.1 \text{ MPa}$, $K_0 = 55 \text{ MPa}$. The energy band structures of the C-T structure and the S-T structure are computed, and the results are depicted in Figs. 1 (c) and (d). From the graphical representations, it is evident that within the unshaded regions, band curves span across frequency ranges, indicating the existence of propagating elastic waves through the respective structures, representing the passbands of the structure. Conversely, the shaded regions represent forbidden bandgaps where corresponding band curves are absent. In this frequency range, acoustic waves cannot propagate through the corresponding structures. Although the C-T and the S-T structures are both chiral PnCs, the energy band structures, which can also be called the dispersion curve, show different characteristics due to the different numbers of curvature segments, which verifies our previous conjecture, and also conforms to the research of a lattice metamaterial composed of sinusoidal beams, where the characterizes the bending quantity of the beams, is directly proportional to the richness of bandgaps [45]. Additionally, it is worth noting that if the region devoid of wave propagation modes spans across all wavevector directions, it is termed a “Complete Bandgap”. Otherwise, it is referred to as a “Directional Bandgap” [27].

Effect of tensile stress on band gap

In the context of tensile loading, both C-T and S-T representative volume elements (RVEs) exhibit sustained periodicity after deformation. To investigate the influence of tensile stress on an individual representative unit, the finite element simulation is employed incorporating periodic boundary conditions and Bloch boundary conditions in the Appendix A. Subsequently, accounting for the effects of pre-stretching, an analysis of the impact of external deformation on the structural bandgap is conducted. The dispersion curves are illustrated in Figs. 2 (a), (c), (e), (g), (i), and (k), with our focus limited to the X-direction bandgap. The analysis of the transmittances for the C-T and the S-T finite structural models serves a dual purpose. It not only characterizes the attenuation properties and attenuation degree of acoustic waves within the structures but also validates the accuracy of the dispersion relationship. The finite element simulation is conducted using steady-state dynamic analysis for frequency sweeping. The structure comprises chiral units and absorbing layers, with excitation and reception at terminals A and B. The chiral unit forms an array of 30×6 units, as described in Fig. 2(m). A sweeping signal in the X-direction is applied to the excitation terminal, resulting in X-direction displacement response values at terminals A and B, denoted as U_A and

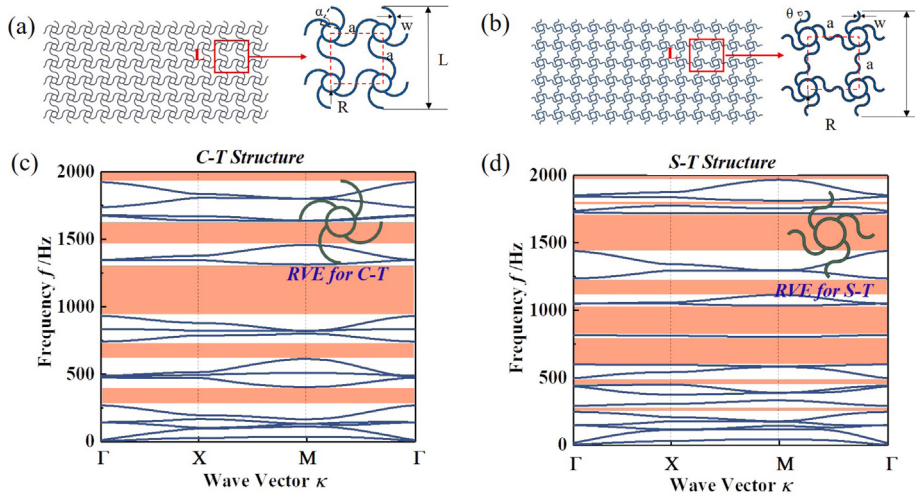


Fig. 1. Two chiral structures named (a) C-T structure and (b) S-T structure, each composed of four ligaments and a circular ring. The energy bands of (c) C-T structure and (d) S-T structure are computed.

U_B , respectively. The transmittance T at a specific frequency can be calculated as follows:

$$T = 20 \log\left(\frac{|U_B|}{|U_A|}\right). \quad (4)$$

The frequency scan range is $0 \text{ Hz} < f \leq 1600 \text{ Hz}$. Similarly, when assessing the response transmittance spectra of a structure subjected to tensile stress, it is imperative to perform large deformation analysis on the structure. Subsequently, the results of stress-strain simulation results on the structure are integrated as the initial conditions for the ensuing transmittance spectrum analysis. In this research, the stretched length of each unit is represented by x . As per the aforementioned Eq. (4), one can obtain the frequency-transmittance response spectra of the structure under various tensile stresses, as depicted in Figs. 2 (b), (d), (f), (h), (j) and (l).

From the aforementioned results, it is evident that the bandgap of the PnC impedes the propagation of sound waves within the structure. Consequently, the transmittance curves exhibit corresponding low values. By comparing the graphs, it can be observed that the transmittance curve obtained from the finite element analysis aligns well with the dispersion curves calculated using the RVEs. This alignment highlights a mutual validation relationship between the band structures and transmittances. The band structure calculations are based on theoretical predictions of the structural dispersion, providing information on the frequency ranges of passbands and stopbands, while transmittances serve to characterize the attenuation performance of the structure at different frequencies when subjected to excitation signals in practical applications. However, it is important to note that the dispersion calculations assume the structure to be an infinitely periodic system, while the transmittance calculations are performed on finite structures. In addition, when the structure is subjected to the tensile stress in the X-direction as the initial condition, the strain of RVE in the Y-direction is almost the same as that in the X-direction. However, for the finite structure, the Y-direction will be constrained by the overall structure, and the strain will increase asymmetrically with the X-direction. Hence, a reasonable level of error is expected within a certain range. By computing the transmittances for two types of chiral structures under varying tensile stresses, a threshold value $T < 0.1$ is defined, indicating significant attenuation at the corresponding frequency, which characterizes the stopband. The results are depicted in Fig. 3, revealing the relationship between the bandgap range and the displacement of unit cells resulting from the applied tensile stress.

As depicted in Fig. 3, as the tensile stress increases and, consequently, the unit cell displacements of both structures gradually grow,

there is a noticeable trend of bandgap shifting towards higher frequencies, the overall bandgap range diminishes progressively, with the S-T structure exhibiting a richer bandgap spectrum when compared to the C-T structure. The above research lays a foundation for extensive applicability in the realms of acoustic wave manipulation, and acoustic devices. Such as acoustic switches and acoustic channels, which are proved in the Appendix B. The attenuation characteristics of structures can be characterized by means of vibration modes. Simulation results show that the structure's isolative and noise attenuation functionalities can be selectively activated or deactivated through the process of tensile stretching, and the purpose of the acoustic switch is realized. Furthermore, the two can be combined to accomplish the function of an acoustic channel.

Logic gate conversion

The forthcoming objective involves the conception of a logic gate that employs a dual-input acoustic wave as input signals, allowing for dynamic alterations of its logical attributes through the act of stretching, there are four-channel arrays 1–4 as depicted in Fig. 4(a). In order to appropriately stimulate this system, a selection of the excitation frequency denoted as f_g indicated by a prominent purple dashed line in Fig. 3 is imperative, $f_g = 1900 \text{ Hz}$. Based on its relationship with the bandgap when $x = 2.5 \text{ mm}$ of the C-T structure and the S-T structure, as shown in Fig. 3. Notably, the S-T structure demonstrates a behavior characterized by “passing when stretched and failing when unstrained”, whereas the C-T structure exhibits a contrasting characteristic of “passing both when stretched and when unstrained”. To emulate the operation of this logic gate, excitation signals are systematically applied to the two input ports, where “1” signifies the application of a signal, while “0” signifies the absence thereof. At the output port, a defined threshold value the normalized $A_m = 0.2$ is introduced, whereby the output registers as “1” only if the received signal amplitude surpasses the threshold A_t and “0” otherwise.

Under conditions where the structure remains devoid of tensile stress, it exhibits AND logic gate behavior, as illustrated in Figs. 4 (a), (b), and (c). In scenarios where both the upper and lower ends are simultaneously stimulated, denoted as input (1, 1). Owing to the attenuation effect exerted by the S-T structures on the incoming signals, acoustic waves predominantly propagate through the central C-T structure. It effectively corresponds to the passage of signals through channels 2 and 3. In this configuration, the output at the receiving end is $A = 0.551$, exceeding the threshold A_m , resulting in an output of 1. When input combinations (1, 0) or (0, 1) are applied, the attenuated

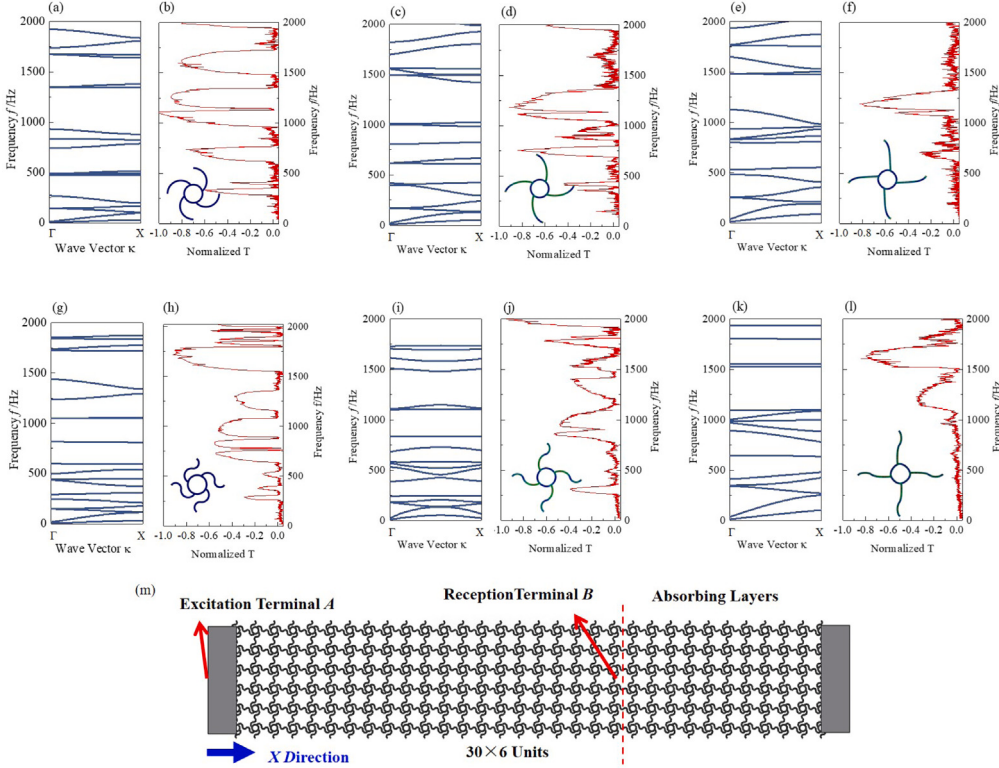


Fig. 2. The dispersion curves and transmittance response spectra for the (a)–(f) C-T structures and the (g)–(l) S-T structures with different stretching: (a)(b)(g)(h) $x = 0$ mm, (c)(d)(i)(j) $x = 1.7$ mm, (e)(f)(k)(l) $x = 2.5$ mm. (m) The finite structural model, the S-T structure is taken for example.

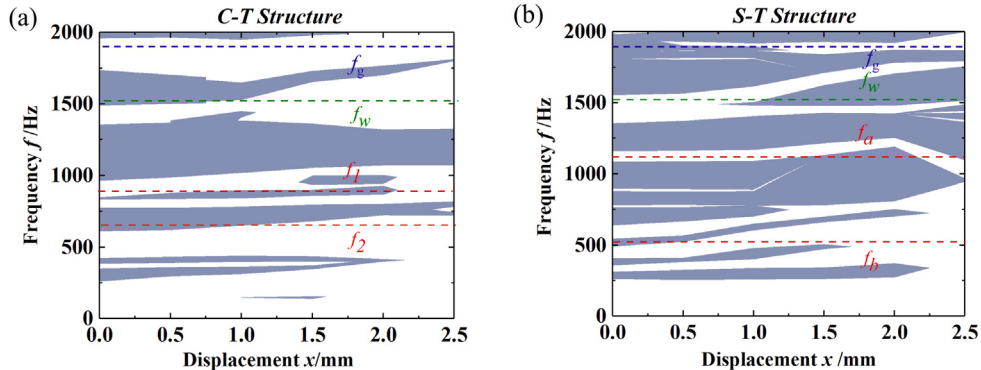


Fig. 3. The variation in PnC bandgaps under the influence of tensile stress for (a) the C-T structure and (b) the S-T structure with identical material and geometric parameters.

excitation signals lead to the activation of only channel 2 or 3. This results in a receiving-end amplitude of $A = 0.123$ and 0.025 , falling below the A_m and yielding an output of 0. In cases where input $(0, 0)$ is implemented, characterized by the absence of excitation signals, there is no propagation of sound waves within the structure, thereby generating an output value of 0. The unstressed structure adeptly embodies the AND logic gate functionality.

Nonetheless, when the structures experience tensile stress ($x = 1.7$ mm), they undergo shifts and alterations in the bandgap positions, enabling the structure to exhibit OR logic gate behavior, as illustrated in Figs. 4 (d), (e) and (f). In the event of an input configuration of $(1, 1)$, all four channels permit the passage of acoustic waves, resulting in a receiving-end amplitude denoted as $A = 0.695$, exceeding the A_t threshold and consequently yielding an output value of 1. For input combinations of $(1, 0)$ or $(0, 1)$, either channels one and two or channels three and four simultaneously allow acoustic wave transmittance, with the output signal's amplitude at $A = 0.507$ and 0.567 , satisfying the threshold criteria and thereby resulting in an

output value of 1. Similarly, when the input is $(0, 0)$, there is a lack of sound wave propagation within the structure, yielding an output value of 0. The stretched structure successfully mimics an OR logic gate's operation.

In essence, for structures under these conditions, the situation where the total energy sum exceeds the threshold only occurs when there are either two (Figs. 5 (a), (e) and (f)) or more than two (Fig. 5(d)) undecayed channels. Figs. 5 (b) and (c) both have one channel experiencing elastic wave decay due to the bandgap and two channels without input signals, resulting in a total output energy below the threshold. The shift from the AND logic gate to the OR logic gate under stretching is also reflected in the received signal normalized amplitudes, as delineated in Fig. 5.

In the antecedent investigation, the acoustic characteristics through the utilization of a two-dimensional (2D) structural model are probed systematically. While the three-dimensional (3D) configuration shares similarities with the 2D counterpart, it is imperative to calculated a 3D model in the finite element simulation based on the same principle

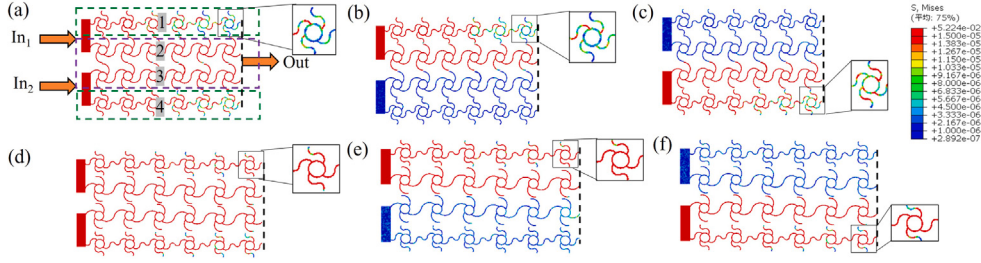


Fig. 4. (a) Tunable logic gate consists of S-T structures enclosed within green frames and C-T structures confined within a purple frame. Two input terminals are denoted as In_1 and In_2 , each interconnected with a respective array of S-T and C-T structures. These structural elements converge at their ends, forming a unified output terminal designated as Out. Simulation results of logic gates under the following structure and input conditions: (a) AND logic gate, input: (1, 1); (b) AND logic gate, input: (1, 0); (c) AND logic gate, input: (0, 1), (d) OR logic gate, input: (1, 1); (e) OR logic gate, input: (1, 0); (f) OR logic gate, input: (0, 1).

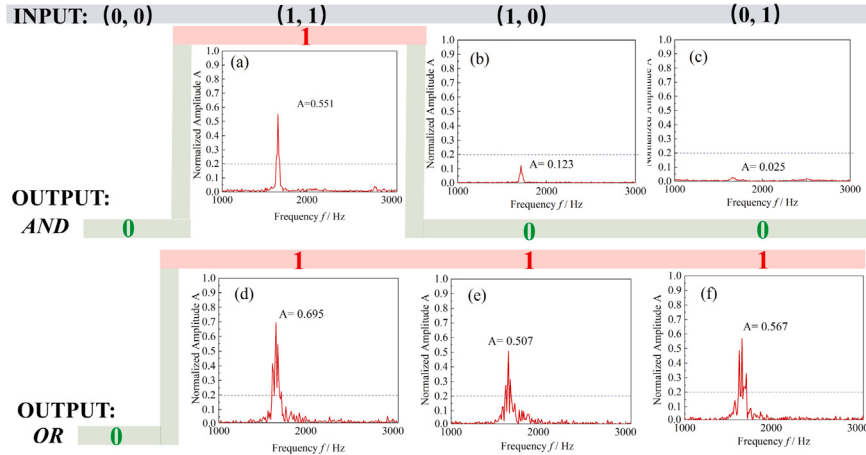


Fig. 5. Received frequency domain signals of the logic gate under the following structure and input conditions: (a) AND logic gate, Input: (1, 1); (b) AND logic gate, Input: (1, 0); (c) AND logic gate, Input: (0, 1). (d) OR logic gate, Input: (1, 1); (e) OR logic gate, Input: (1, 0); (f) OR logic gate, Input: (0, 1).

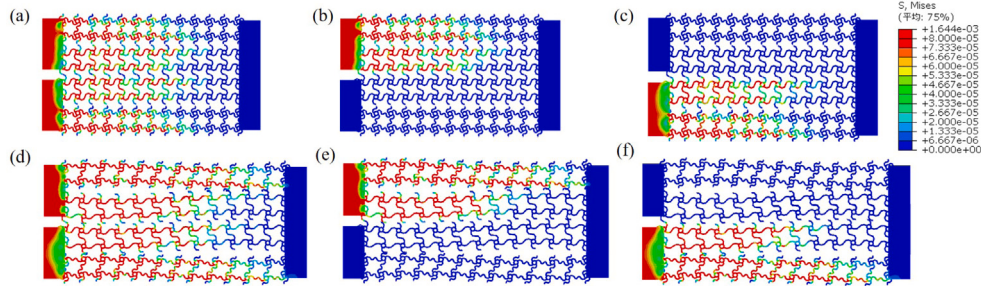


Fig. 6. Simulation results verified the experiment of logic gates under the following structure and input conditions: (a) AND logic gate, input: (1, 1); (b) AND logic gate, input: (1, 0); (c) AND logic gate, input: (0, 1). (d) OR logic gate, input: (1, 1); (e) OR logic gate, input: (1, 0); (f) OR logic gate, input: (0, 1).

of controllable logic gate. The selection of materials is explained in the Appendix C. Prior studies aimed to select a sufficient number of unit cells to approach the ideal PnC structure with an infinite number of unit cells. However, in order to meet the requirements of the subsequent experiment, taking practical considerations into account, the structures with 30, 25, 20, and 15 rows of unit cells are chosen for our investigation. The results indicate that the structures with 15 rows of unit cells satisfy the requirements for studying bandgap variations under tension. Considering the process of the test specimen and test conditions, the thickness $h = 4$ mm, strap width $w = 1$ mm, $f_g = 160$ Hz. The simulation results are as shown in Fig. 6.

Under these conditions, the research only pay close attention to the distribution of energy. All channels are bandgaps when not stretched, as shown in Fig. 6(a), but due to finite channel lengths, complete attenuation does not occur. Therefore, only when all channels have elastic

waves entering, the total energy of all the channels is spectacular. As shown in Figs. 6 (b) and (c), the total energy will show a low value state due to the reduction of output ports. Therefore, the 1, 0, 0 output of the AND logic gate is presented separately. After stretching, the S-T structure becomes a passband, and the energy distribution graph indicates longer transmission distances, as shown in Figs. 6 (d) (e) and (f). Thus, with only one input port, the total output energy can reach a high dose which perform the OR logic gate. It is worth noting that the restricted quantity of units is the cause of the asymmetric energy transfer of the same kind of chiral structure in Fig. 6, and the tentacles of the unit connected to the input end will display different contact areas of input end depending on whether the line is close to the edge. All in all, Fig. 6 clearly obtain the tunable logic gate and the propagation process of elastic wave in the structure.

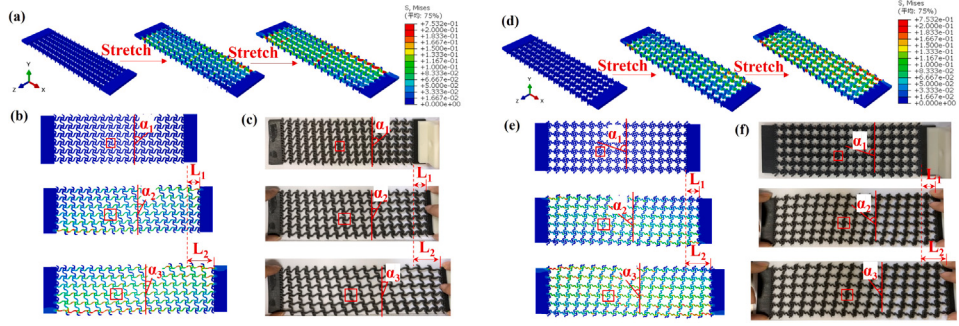


Fig. 7. The 3D finite element tensile model and experimental tensile results for the (a) (b) (c) C-T structure and (d) (e) (f) S-T structure. (a) (d) Emulational deformation and stress distribution for three scenarios: undeformed, $L_1 = 25.5$ mm and $L_2 = 37.5$ mm. Depict corresponding (b) (e) simulated top views and corresponding (c) (f) experimental top views.

Experiment

An enumerative sum of 15 unitary units are decided as the empirical parameters in order to manufacture 3D printing specimens as shown in Figs. 7 (c) and (f). The thickness $h = 4$ mm, the strap width $w = 1$ mm. The deformation of the C-T structure obtained by experiment and simulation during stretching are shown in Figs. 7 (a), (b) and (c). A completely fixed boundary is applied to the left end, and an X-direction tension is applied to the right side. L_i ($i = 1, 2$) is the total structure's stretched length. A comparison highlights that when subjected to tensile stress, chiral structures rotate with respect to centers, represented by the angle $\alpha_1 > \alpha_2 > \alpha_3$, and the ligaments are elongated both laterally and vertically, as indicated by the boxed regions in Fig. 7(a) and (b). As the width of the stress in the X-direction increases, there is also an expansion in the Y-direction, which characterizes the negative Poisson ratio. The experimental deformation of the chiral curved unit cells under lateral tensile stress bespeaks a remarkable congruity with the simulation results, similarly in the S-T structure depicted in Figs. 7 (d), (e), and (f). In the experiments, non-uniform deformation at the upper and lower edges is observed during sample stretching, which is attributed to the finite size of the structures.

The experimental layout and system are explicitly delineated in Fig. 8(a). All experimentations in this study are exclusively conducted upon an optical platform (LSXPT). The signal generation is executed through a precision signal generator (VICTOR, 2040H), and the resultant sinusoidal waveforms are subsequently subjected to a power amplifier (BUYSSENSOR, HJZT-100). The augmented signals are then channeled to excite a transducer (BUYSSENSOR, HGXY100) for the purpose of inducing horizontal lateral vibrations. To ensure the uniform propagation of plane waves through the structure, a purpose-designed connector block, is attached to the sample ends. The transducer's linkage is secured to the specimen using screws and nuts, and at the 6th column unit of the specimen, a receiving card is attached to serve as the receiving terminus, as depicted in Fig. 8(b). Elastic wave signals at the transmitter and receiver ends are measured using a laser vibrometer (Polytec). The laser vibrometer comprises three main components: a laser probe (Polytec, OFV534), a laser switch (Polytec, OFV534), and a vibration control unit (Polytec, OFV-5000). The signals acquired by the laser vibrometer are displayed and recorded using an oscilloscope (Agilent, DSO9104 A). In order to guarantee that the elastic waves incident vertically on the sample surface and that the laser vibrometer and specimen remained in the same horizontal plane, the sample and laser probe are placed on adjustable experimental platforms. Notably, the initial six units are suspended to minimize friction between the sample and the platform, thus reducing potential interference.

The experimental excitation frequency spanned a range from 10 Hz to 1300 Hz. In Fig. 9(a), a comparison unfolds, juxtaposing the experimental results and the simulation results of the elastic wave transmittance for the C-T structure without tension, which revealed fairly

similar band gap characteristics whose primary bandgap is B_1 , and additional bandgaps are $b_1 - b_3$. Fig. 9(b) affords a comparison between the experimental and simulation results of the S-T structure. The agreement between the two sets of results is notably strong. The S-T structure exhibits primary bandgaps denoted as B_1 and B_2 , along with additional bandgaps $b_1 - b_3$, surpassing the number of bandgaps found in the C-T structure, consistent with the previously mentioned simulation results.

In the experiment, the receiving signal is positioned in the 6th column, while columns 7–15 on the experimental platform provided friction to act as an absorbed layer for the transmitted elastic wave, which forestalling the cascade of reflective waves from the structural terminus. Further inquiry into the relationship between bandgap distribution and structural tension is conducted, as illustrated in Figs. 10 (a) and (b). In the absence of applied tensile stress, the transmittance displays an overall lower value, aligning consistently with our simulation findings in Fig. 9. After the application of tension (as indicated by the blue and red curves), the low-value region of the transmittance diminishes, accompanied by a reduction in the number of bandgaps and a narrowing of the primary bandgap. This outcome implies that the capability to manipulate both the number of bandgaps and the propagation characteristics of elastic waves through the application of tensile stress is possessed. A unique frequency, $f_g = 160$ Hz, is chosen for demonstration. The designations T_1 , T_2 , and T_3 in Figs. 10(a) and (b) signify the features of signals within the transmittance spectrum, as subsequently depicted in Figs. 10 (c) and (d).

Notably, when elastic waves traverse the C-T structure, there is a pronounced attenuation, reaching 94%. This observation suggests that the frequency is situated within the bandgap. Upon stretching the structure, the red curve corresponds to $x = 1.7$ mm, revealing a reduced degree of attenuation for the elastic wave at 68.9%. The blue curve, representing $x = 2.5$ mm, exhibits an attenuation rate of 51.7%, notably lower than that at $x = 1.7$ mm. This implies a shift in the dispersion curve after stretching, causing the frequency to exit the bandgap. It is worth highlighting that due to the substantial damping characteristics of rubber-like materials, elastic waves experience noticeable attenuation, even within the passband, which demands due consideration. The attenuation rates for the S-T structure under three conditions, unstretched, $x = 1.7$ mm, and $x = 2.5$ mm, are as follows: 79.5%, 79.3%, 80.1%. It can be inferred that both before and after stretching, the frequency remains within the bandgap. Disregarding the bandgap issue, the elongation of the S-T structure should theoretically increase the elastic wave's path and lead to greater attenuation. However, the results here indicate a reduction, suggesting that it is not due to conventional elastic wave propagation attenuation. The attenuation rate of the C-T structure increases significantly following tension, in contrast to the distinctive pattern observed in the S-T structure. This discrepancy underscores that, in our experiment, the decay of elastic waves is not contingent on propagation distance but is contingent upon the bandgap mechanism engendered by the periodic PnC structure.



Fig. 8. Experimental system. (a) Photograph of the experimental arrangement. (b) The specimen and the exciter are connected by nuts, and the input end, output end, connector block, and receiving card are marked; (c) The specimen is stretched by moving the position of the experimental lifting platform.

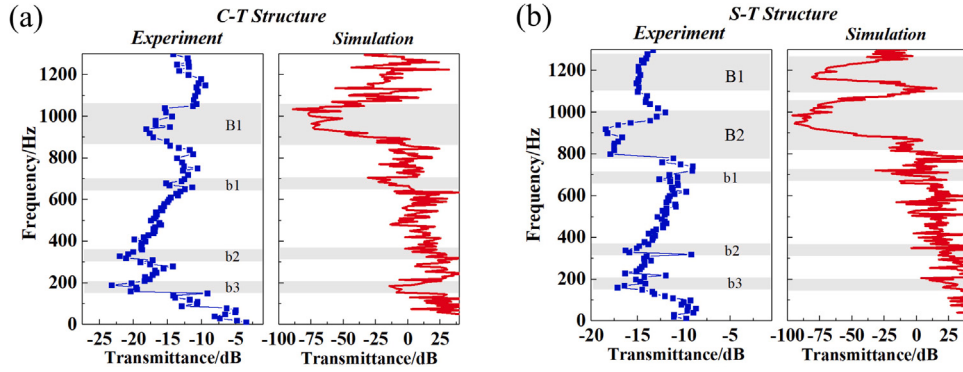


Fig. 9. A comparison between experimental and simulated results regarding the representation of (a) the C-T structure and (b) the S-T structure band gaps by transmittances.

Within the same experimental system mentioned previously, the logic gate test specimens, as illustrated in Fig. 11(a), exhibit familiar traits. S-T and C-T structures are encased within red frames and green frames, respectively, while In_1 and In_2 denote the input terminals, and Out signifies the output terminal. As delineated in Fig. 11(b), the experimental setup characterizes logic gate inputs as (0, 0), (0, 1), (1, 0), and (1, 1) using distinct loading configurations. For the input configuration (0, 0), both input terminals remain void of vibrational excitation, consequently preventing elastic wave propagation within the specimen, thereby consistently yielding an output of 0. This case will not be further discussed. Conversely, when the input (1, 1) is introduced, a connecting element unifies the exciter links of both input terminals, ensuring the concurrent presence of elastic waves, both in terms of magnitude and direction. The amplitude at the output terminal is quantified, with the receiving points positioned at the center of the Out port. Take, for instance, an excitation frequency of $f_g = 160$ Hz is established, according to the frequency of the elastic wave, select the threshold $Am = 15$ mV with the best application effect. Should the received amplitude exceed Am , the output is designated as 1; conversely, an amplitude below Am designates an output of 0.

As shown in Fig. 11(c), when the inputs are (0, 0), (0, 1), (1, 0), and (1, 1), prior to stretching (indicated in green), elastic wave attenuation is readily apparent. This attenuation arises from the notably lower transmittances associated with both the C-T and S-T structures at 160 Hz. Notably, the received amplitude only approaches the threshold when there is vibration at both input ends, resulting in outputs of 0, 0, 0, and 1, effectively realizing the AND function. In contrast, after stretching (indicated in red), a phenomenon attributed to bandgap shifts and alterations, also evidenced in Fig. 10, transpires, significantly increasing the transmittances at this frequency. Notably, substantial elastic wave attenuation occurs solely during transit through the S-T structure. Consequently, with only one input port, the amplitude at the output terminal can surpass the threshold, yielding outputs of 0, 1, 1,

and 1, thus achieving the OR function. The experiment demonstrated the transformation of the samples AND logic gate to an OR logic gate through stretching. Contrast the results and the analyzes with the finite element simulations of the 3D structure in experimental settings in Fig. 6. The experimental results are also carried out to verify the Finite element simulations.

The presence of experimental errors is an inevitable aspect of the study. Notably, the transmittance values may not align perfectly, these disparities, however, remain fall within the acceptable spectrum, refraining from deciding the discernment of bandgap values, this discrepancy can be attributed to primary factors: firstly, the damping coefficients applied in simulations are estimates, while the experimental damping coefficients subject to factors such as temperature and humidity. Secondly, while the experiment ensures consistent output voltage and amplification factors at different frequencies, the energy required to excite motion at the connection rod varies with frequency. Thus, at low frequencies, amplitude surges while, at high frequencies, it wanes. This variation in amplitude cannot be ruled out as a potential influence on the transmittance. Furthermore, the intrinsic weight of the samples and the inability to receive signals within the structure's interior due to adhesive bonding at a certain height are also sources of error.

Conclusion

In conclusion, by introducing the controllable chiral PnCs, a new way to mold the tunable acoustic logic gate is distinct from the conventional immutable logic gates. Due to disparities in the number of curvature segments within the C-T and S-T structures, the mechanical stretching imparts analogous yet divergent characteristics in terms of bandgap shifts and modifications. The propagation of acoustic waves within the structure can be deftly controlled through the stretching of C-T and S-T configurations. This paper introduces various combinations

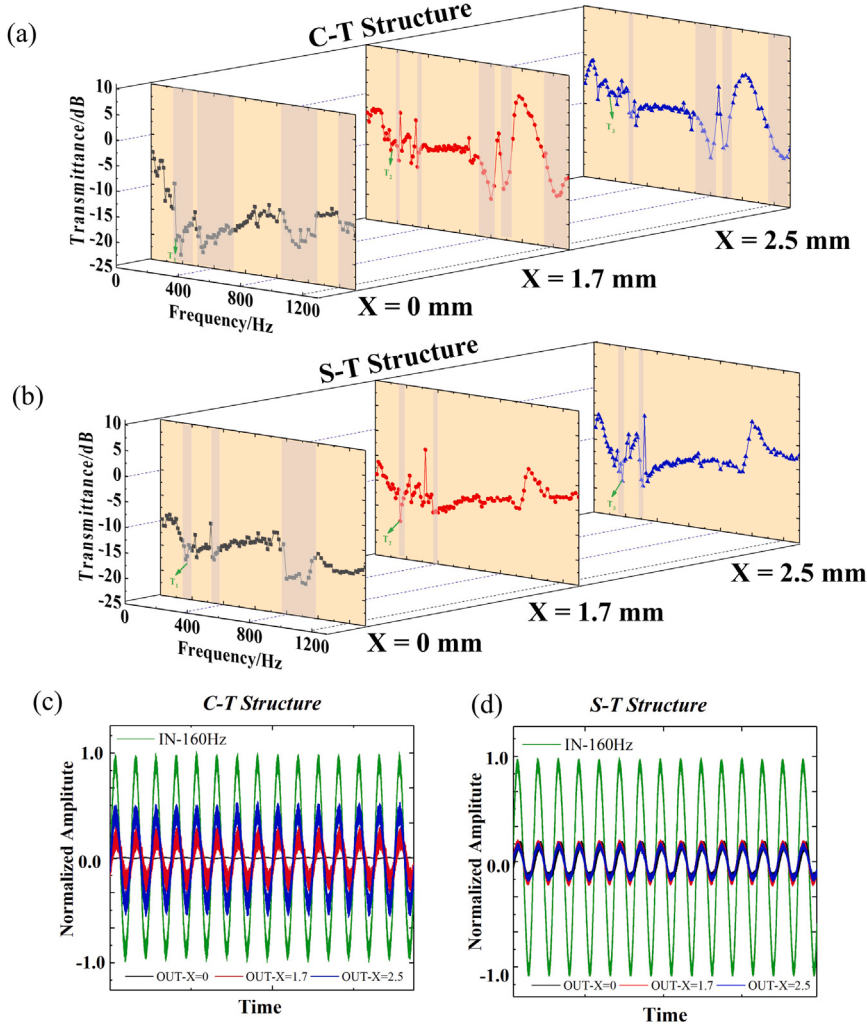


Fig. 10. Comparison of the experimental results of the transmittance spectra of (a) the C-T structure and (b) the S-T structure under different tensile conditions. Receiving elastic wave signals in (c) C-T and (d) S-T structures at 160 Hz excitation frequency.

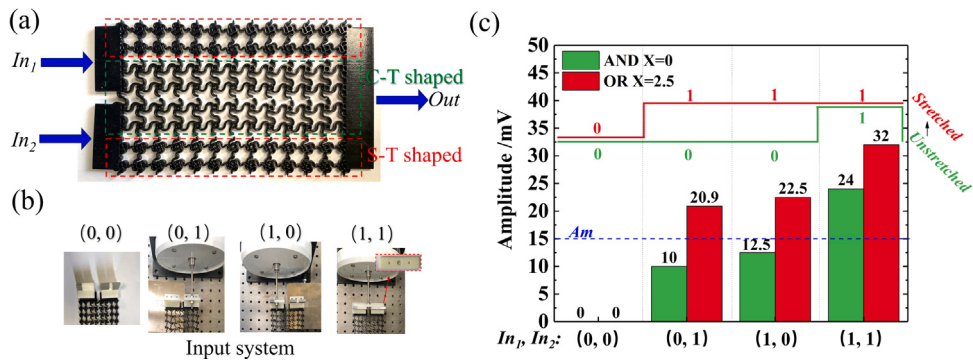


Fig. 11. (a) The logic gate test specimen. (b) The experimental setup characterizes logic gate inputs as (0, 0), (0, 1), (1, 0), and (1, 1) using distinct loading configurations. (c) When the inputs are (0, 0), (0, 1), (1, 0), and (1, 1), receiving elastic wave amplitude prior to stretching (indicated in green) and after stretching (indicated in red), they are represented as AND and OR logic gates.

of these structures, substantiated by the finite element simulations and experimental validation, to realize the swift transition of acoustic devices and tunable logic gates. Consequently, the research outlined in this study marks a significant breakthrough in the field of acoustic devices. However, in order to improve the comparability of logic gate output results, a material with low damping and high deformation is required to be deeply researched and replace the soft materials with high attenuation.

CRediT authorship contribution statement

Yuanyuan Li: Conceptualization, Methodology, Software, Formal analysis, Writing – original draft, Investigation. **Kunqi Huang:** Software, Validation, Data curation. **Menyang Gong:** Data curation, Investigation. **Chenghao Sun:** Formal analysis. **Shenlian Gao:** Data curation. **Yun Lai:** Methodology, Supervision. **Xiaozhou Liu:** Funding acquisition, Writing – review & editing, Project administration, Resources, Supervision.

Declaration of competing interest

The authors declare that they have no known competing financial interests or personal relationships that could have appeared to influence the work reported in this paper.

Data availability

Data will be made available on request.

Acknowledgments

This project was funded by the National Key R&D program of China (Grant No. 2020YFA0211400), the State Key Program of National Natural Science of China (Grant No. 11834008), the National Natural Science Foundation of China (Grant No. 12174192, No. 11974176, No. 12174188), the State Key Laboratory of Acoustics, Chinese Academy of Sciences (Grant No. SKLA202210), the Key Laboratory of Underwater Acoustic Environment, Chinese Academy of Sciences (Grant No. SSHJ-KFKT-1701).

Supplementary data

Supplementary material related to this article can be found online at <https://doi.org/10.1016/j.rinp.2024.107421>.

References

- [1] Li F, Anzel P, Yang J, Kevrekidis PG, Daraio C. Granular acoustic switches and logic elements. *Nature Commun* 2014;5:5311.
- [2] Bilal OR, Foehr A, Daraio C. Bistable metamaterial for switching and cascading elastic vibrations. *Proc Natl Acad Sci USA* 2017;114:4603.
- [3] García-Pablos D, Sigalas M, de Espinosa FRM, Torres M, Kafesaki M, García N. Theory and experiments on elastic band gaps. *Phys Rev Lett* 2000;84:4349.
- [4] Zhang S, Zhang Y, Guo YJ, Leng YH, Feng W, Cao WW. Realization of subwavelength asymmetric acoustic transmission based on low-frequency forbidden transmission. *Phys Rev A* 2016;5:034006.
- [5] Lloyd J, Ludwikowski C, Phansalkar D, Malik C, Shen C. 3D printed acoustic metamaterial filters for the mitigation of inaudible ultrasound attacks on smart speakers. *J Acoust Soc Am* 2023;153:A197.
- [6] Tang S, Wu JL, Lv C, Song J, Jiang YY. Functional acoustic metamaterial using shortcut to adiabatic passage in acoustic waveguide couplers. *Phys Rev A* 2022;18:014038.
- [7] Bringuera S, Swinteck N, Vasseur JO, Robillard JF, Runge K, Muralidharan K, et al. Phase-controlling phononic crystals: Realization of acoustic Boolean logic gates. *J Acoust Soc Am* 2011;130:1919.
- [8] Zhang T, Cheng Y, Guo JZ, Xu JY, Liu XJ. Acoustic logic gates and boolean operation based on self-collimating acoustic beams. *Appl Phys Lett* 2015;106:113503.
- [9] Víctor E, Víctor SM, Kestutis S, Isabel PA, Javier R. Subdiffractive propagation of ultrasound in sonic crystals. *Phys Rev B* 2007;76:140302.
- [10] Alagoz S, Alagoz BB. Sonic crystal acoustic switch device. *J Acoust Soc Am* 2013;133:EL485.
- [11] Cicek A, Kaya OA, Ulug B. Impacts of uniaxial elongation on the bandstructures of two-dimensional sonic crystals and associated applications. *Appl Acoust* 2012;73:28.
- [12] Lan J, Wang LW, Zhang XW, Lu MH, Liu XZ. Acoustic multifunctional logic gates and amplifier based on passive parity-time symmetry. *Phys Rev A* 2020;13:034047.
- [13] Rajesh A, Viswanathan B, Nafisa N. A reversible bimodal joint nimbly optical logic gate using photonic crystals. *J Opt-UK* 2021;23:125001.
- [14] Amaria IS, Palacio G, Tripathy S, Nayake S. Realisation of all photonic logic gates using plasmonic-based photonic structure through bandgap analysis. *Optik* 2019;194:163123.
- [15] Zhang YL, Zhang Y, Li BJ. Optical switches and logic gates based on self-collimated beams in two-dimensional photonic crystals. *Opt Express* 2007;15:9287.
- [16] Zhao DY, Zhang J, Yao PJ, Jiang XY. Photonic crystal Mach-Zehnder interferometer based on self-collimation. *Appl Phys Lett* 2007;90:231114.
- [17] Goffaux C, Vigneron JP. Theoretical study of a tunable phononic band gap system. *Phys Rev B* 2001;64:075118.
- [18] Yang AC, Li P, Wen YM, Lu CJ, Peng X, Zhang JT, et al. Significant tuning of band structures of magneto-mechanical phononic crystals using extraordinarily small magnetic fields. *Appl Phys Lett* 2014;105:011904.
- [19] Walker E, Reyes D, Rojas MM, Krokhin A, Wang ZM, Neogi A. Tunable ultrasonic phononic crystal controlled by infrared radiation. *Appl Phys Lett* 2014;105:143503.
- [20] Huang ZG, Wu TT. Temperature effect on the bandgaps of surface and bulk acoustic waves in two-dimensional phononic crystals. *IEEE Trans Ultrason Ferr* 2005;52:365.
- [21] Airolidi L, Ruzzene M. Design of tunable acoustic metamaterials through periodic arrays of resonant shunted piezos. *New J Phys* 2011;13:113010.
- [22] Li B, Cao YP, Feng XQ, Gao HJ. Mechanics of morphological instabilities and surface wrinkling in soft materials: a review. *Soft Matter* 2012;8:5728.
- [23] Li YY, Liu JC, Deng ZY, Gong MY, Huang KQ, Lai Y, et al. Acoustic three-terminal controller with amplitude control for nonlinear seismic metamaterials. *AIP Adv* 2022;12:075312.
- [24] Jin Y, Fernez N, Pennec Y, Bonello B, Moiseyenko RP, Hénon S, et al. Tunable waveguide and cavity in a phononic crystal plate by controlling whispering-gallery modes in hollow pillars. *Phys Rev B* 2016;93:054109.
- [25] Jin Y, Pennec Y, Pan Y, Djafari-Rouhani B. Phononic crystal plate with hollow pillars connected by thin bars. *J Phys D Appl Phys* 2017;50:035301.
- [26] Bertoldi K, Boyce MC. Wave propagation and instabilities in monolithic and periodically structured elastomeric materials undergoing large deformations. *Phys Rev B* 2008;78:184107.
- [27] Bertoldi K, Boyce MC. Mechanically triggered transformations of phononic band gaps in periodic elastomeric structures. *Phys Rev B* 2008;77:052105.
- [28] Bertoldi K, Boyce M, Deschanel S, Prangea S, Mullin T. Mechanics of deformation-triggered pattern transformations and superelastic behavior in periodic elastomeric structures. *J Mech Phys Solids* 2008;56:2642.
- [29] Shim JM, Wang P, Bertoldi K. Harnessing instability-induced pattern transformation to design tunable phononic crystals. *Int J Solids Struct* 2015;58:52.
- [30] Wang P, Casadei F, Shan S, Weaver JC, Bertoldi K. Harnessing buckling to design tunable locally resonant acoustic metamaterials. *Phys Rev Lett* 2014;113:014301.
- [31] Ning SW, Chu DY, Jiang H, Yang FY, Liu ZL, Zhuang Z. The role of material and geometric nonlinearities and damping effects in designing mechanically tunable acoustic metamaterials. *Int J Mech Sci* 2021;197:106299.
- [32] Xin XZ, Liu LW, Liu YJ, Leng JS. 4D printing auxetic metamaterials with tunable, programmable, and reconfigurable mechanical properties. *Adv Funct Mater* 2020;30:2004226.
- [33] Ha CS, Plesha ME, Lakes RS. Chiral three-dimensional lattices with tunable Poisson's ratio. *Smart Mater Struct* 2016;25:054005.
- [34] Grima JN, Gatt R, Farrugia PS. On the properties of auxetic meta-tetrachiral structures. *Phys Status Solidi B* 2008;245:511.
- [35] Alderson A, Alderson K, Attard D, Evans K, Gatt R, Grima J, et al. Elastic constants of 3-, 4- and 6-connected chiral and anti-chiral honeycombs subject to uniaxial in-plane loading. *Compos Sci Technol* 2010;70:1042.
- [36] Hamid E, Davood M, Hamid NH, Julian N, Ashkan V. 3D cellular metamaterials with planar anti-chiral topology. *Mater Des* 2018;145:226.
- [37] Wang W, Lv SC, Xu W, Bai L. Multi-objective optimization of thermal expansion and adjustable band gap for a chiral triangular lattice metamaterial. *Arch Appl Mech* 2022;92:3967.
- [38] Spadoni A, Ruzzene M, Gonella S, Scarpa F. Phononic properties of hexagonal chiral lattices. *Wave Motion* 2009;46:435.

- [39] Chen LY, Liu Y, Kong H. Acoustic tunneling study for hexachiral phononic crystals based on Dirac-Cone dispersion properties. *Crystals* 2021;11:1577.
- [40] Gent AN. A new rubber chemistry and technology, constitutive relation for rubber. *Rubber Chem Technol* 1996;69:59.
- [41] Rivlin RS. Large elastic deformations of isotropic materials. IV. Further development of the general theory. *Philos Trans R Soc, A* 1948;241:379.
- [42] Yeoh OH. Characterization of elastic properties of carbon black filled rubber vulcanizates. *Rubber Chem Technol* 1990;63:729.
- [43] Mooney M. A theory of large elastic deformation. *J Appl Phys* 1940;11:582.
- [44] Chou-Wang MS, Horgan CO. Void nucleation and growth for a class of incompressible nonlinearly elastic materials. *Int J Solids Struct* 1988;25:1239.
- [45] Chen YY, Li TT, Scarpa F, Wang LF. Lattice metamaterials with mechanically tunable poisson's ratio for vibration control. *Phys Rev A* 2017;7:024012.